AIAA JOURNAL
Vol. 47, No. 3, March 2009

Nonlinear Analytical Approach for Preliminary Sizing of Discrete Composite Stringer Terminations

Enzo Cosentino*
Airbus UK, Ltd., Bristol, England BS99 7AR, United Kingdom
and
Paul M. Weaver†
University of Bristol, Bristol, England BS8 1TR, United Kingdom

DOI: 10.2514/1.37745

A recently developed nonlinear approach is adapted and used to predict crack initiation in stringer terminations of discretely assembled composite panels made from skin and stiffeners. A linear elastic fracture mechanics based submodel is used to simulate the crack initiation in the critical regions and the influence of ply drop-off is captured. The von Kármán formulation for moderately large deflections in plates is used to capture the nonlinear structural behavior; three-dimensional assemblies are schematized and the effect of eccentricity is included in the simulation. An optimum design criterion is sought and basic guidelines for good design are provided. Furthermore, a method for preliminary assessment of structural strength is proposed and predictions are validated against detailed nonlinear finite element analysis.

Nomenclature

C_M	=	bending moment constant
C_N	=	in-plane load constant
E_{fe}	=	equivalent elastic modulus of tapered region of foot with ply drop-off
e	=	neutral plane function
e_i	=	generalized coordinates of the neutral plane function
G_{IC}	=	critical strain energy release rate for mode I
G_{IIC}	=	critical strain energy release rate for mode II
G_{IN}, G_{IM}	=	local strain energy release rate contribution upon mode I due to in-plane loads and bending moments
G_{IIN}, G_{IIM}	=	local strain energy release rate contribution upon mode II due to in-plane loads and bending moments
L	=	length of panel
N, M	=	in-plane loads and bending moment resultants
t_{fe}	=	equivalent thickness of tapered region of foot with ply drop-off
U	=	internal elastic potential energy
$U_{\text{DO},N}$	=	internal elastic potential energy due to in-plane load in drop-off area
$U_{\text{DO},M}$	=	internal elastic potential energy due to in bending in drop-off area
u	=	in-plane displacement in x direction
w	=	out-of-plane displacement
w_i	=	generalized coordinates of the displacement function
$\varphi_{e,i}$	=	eccentricity eigenfunctions
φ_i	=	beam eigenfunctions
Ω_N	=	potential of external in-plane loads
Ω_Q	=	potential of external transverse loads

Presented as Paper 1919 at the 49th AIAA/ASME/ASCE/AHS/ASC Structures, Structural Dynamics, and Materials Conference, Schamburg, IL, 7–10 April 2008; received 27 March 2008; revision received 29 September 2008; accepted for publication 18 October 2008.

*Composite Stress Analysis, Composite Structures Development Centre; enzo.cosentino@airbus.com.

†Reader, Advanced Composite Centre for Innovation and Science, Department of Aerospace Engineering, Queens Building 2.39, University Walk. Member AIAA.

I. Introduction

IT IS well known that the use of co-cured, co-bonded, and secondary bonded composite structures offers significant potential for weight reduction over conventional bolted metallic designs. The superior performance and competitiveness of carbon fiber reinforced plastics against conventional metals are due, in part, to the greater number of parameters that designers can tailor to meet mission deliverables. If the greater number of variable parameters increases the degree of adaptability of such structures, then the tailoring and optimization processes require a deeper level of understanding and additional computational effort. As a consequence, there may be a conflict with the restricted time scales required by the current market trend. With the new era of "total-carbon design" launched by the novel Airbus A350-XWB and Boeing 787, the aerospace industry is facing new challenges and a variety of novel issues are still to be resolved by designers. The present work focuses its attention on the terminations of composite stringers bonded to composite skins, and, in particular, on the shape of discrete assemblies. This design solution offers significant improvements to manufacturing in terms of cost, time, and ease. Nevertheless, the vulnerability of such structures to through-thickness stresses is well known. Stringer run-outs are critical design areas. The combination of several mechanical and geometrical parameters, coupled with the lack of complete understanding, renders the problem difficult and complex. Stiffened panels are core subcomponents of almost all aircraft components such as wing, empennage, and fuselage structures. The susceptibility to interlaminar damage is particularly exacerbated in thick-sectioned run-out regions that usually characterize wing designs, where stringers must be run out due to design restrictions. Tapering the stringer web and running it out at the rib or spar's flange [1,2] is the most commonly accepted technique.

The tapered design, illustrated in Fig. 1, guarantees a smoother mechanical load transfer from the skin to the stringer and is readily achievable from a manufacturing perspective. Furthermore, the smoother eccentricity (Fig. 2) of the in-plane loads with respect to the local neutral plane of the terminated stringer reduces local bending. Recent studies [3–5] have shown that primary attention should be given to the skin/stringer bond line at the termination tip,

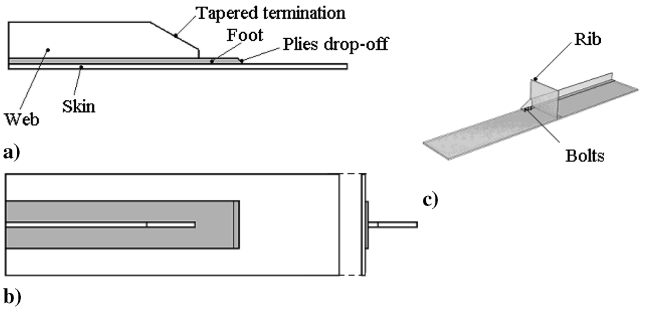

Fig. 1 Typical discrete run-out design solution.

as shown in Fig. 3c. Apparently, terminating the stiffener at the rib or spar's flange (Fig. 1c) seems to provide partial relief to the pure peeling stresses triggered at the run-out tip, hence providing a benefit to the structure.

However, crack initiation due to the pure peeling mode (mode I) is not necessarily the main cause of failure. Greenhalgh and Huertas-Garcia [5] have shown, for the analyzed configurations, that damage initiation was due to a mode I dominated intralaminar fracture arising at the skin surface (refer to the notation used in Fig. 1). However, the influence of mode II increased as the crack front advanced, leading to a mixed mode delamination growth. Cosentino and Weaver [1] employed the linear elastic fracture mechanics (LEFM) model developed by Williams [6] in combination with a nonlinear Ritz-based formulation and a Galerkin technique to model the eccentricity function, and applied both submodels to predict crack initiations in simple stringer termination specimens tested by Falzon and Davies [3].

Such specimens show that there is not a typical failure mode. Failure may occur due to mode I, mode II, or a mixed mode governed crack initiation.

The presence of the constraint from the two ribs and adjacent stringers (Fig. 2) defines the bay in which the stringer is run out. The combination of material properties and the transverse bending/axial stiffness proportions between skin and stringer may strongly influence the sign of the local curvature at the tip datum, thus triggering (and partitioning accordingly) the loads' contributions upon modes I and II and causing any of several possible failure modes characterized by significantly different failure loads (Figs. 4 and 5).

Because of the eccentricity, the in-plane load induces a local curvature that, depending on its sign, could produce a peeling moment that coalesces with pure sliding (mode II). It is noteworthy that the in-plane load is always present. In fact, the primary load in wing covers is the local in-plane load due to global bending of the wings. Its contribution is a significant pure sliding fracture mode. Nevertheless, the magnitude and the sign of local curvature at the tip, which determines the size of the local bending moment to be partitioned, may represent the most important variable. Referring to Fig. 1 for the typical geometry and to Figs. 4 and 5, the following conventions are introduced:

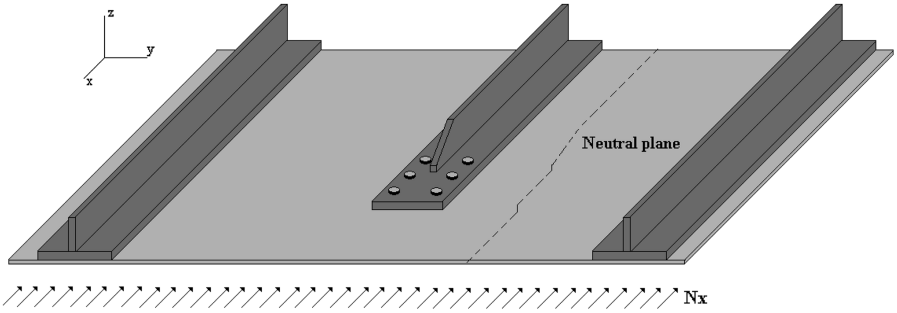

Fig. 2 Typical one-bay panel including stringer termination. The boundaries are defined chordwise by the two stringers 1 and 3, and lengthwise by forward and backward rib datums.

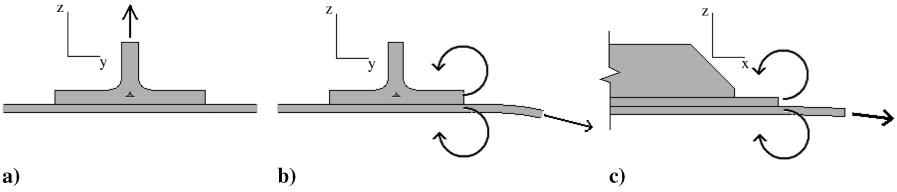

Fig. 3 a) Noodle failure mode, b) lateral failure, and c) tip failure mode.

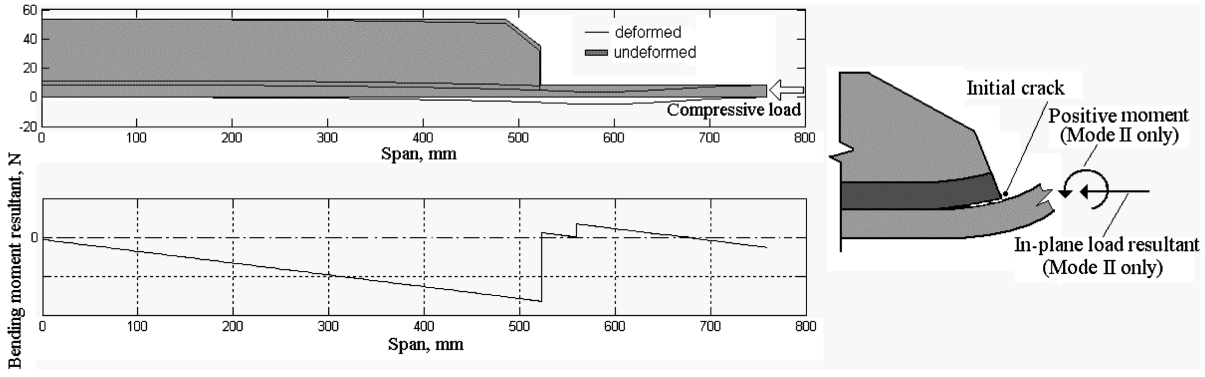

Fig. 4 Example of initial crack due to a combination of a positive local bending and the in-plane load resultant. The initiation is solely mode II governed.

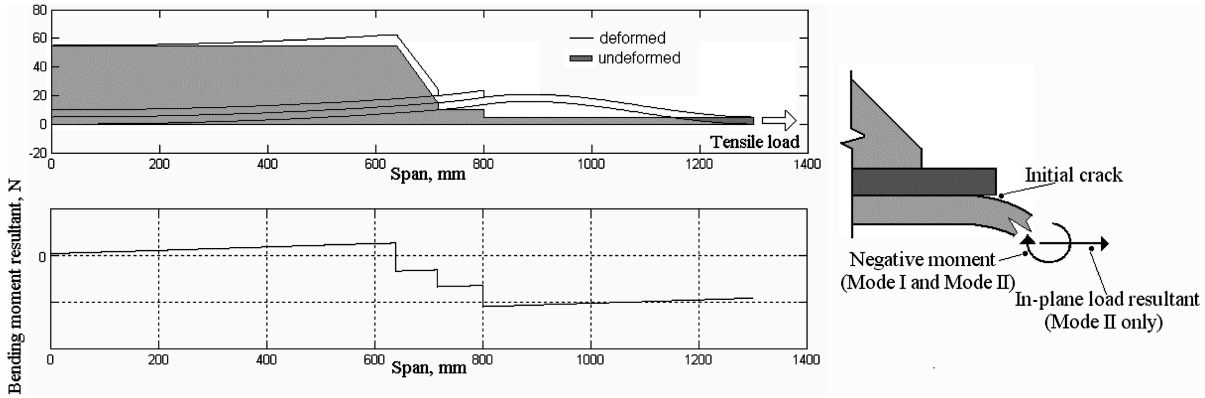

Fig. 5 Example of initial crack due to a combination of a negative local bending and the in-plane load resultant. The initiation is due to an interaction of modes (mixed modes).

1) *Positive curvature* (Fig. 4): no contribution of mode I is triggered and the structure shows higher failure loads.

2) *Negative curvature* (Fig. 5): it is the worst case. The contribution of mode I is triggered proportionally to the amount of locally induced curvature. The structure shows appreciably lower failure loads.

In the present study, it is assumed that the in-plane load triggers the mode II failure only, and the amount of the mode II excitation does not depend on the sign (tension of compression). It is also assumed that the transverse bending moment is potentially able to excite both modes I and II, and that the mode I component vanishes only in the case represented in Fig. 4 (positive curvature). The contribution of mode III to the crack initiation, as well as the effect of the transverse shear resultant, is neglected. The latter effect in fact does not significantly contribute to the initial failure as shown in the following sections.

The assumptions imply that, potentially, three subclasses of failure work simultaneously: 1) mode I component due to the transverse secondary bending; 2) mode II component due to the transverse secondary bending; and 3) mode II component due to the in-plane load.

Several design solutions have been developed, implemented, and tested to challenge the failure mechanisms by partially relieving the local stress concentration. For instance, the first and simpler proposed solution is schematized in Fig. 6a. Pretensioned bolts are used to help the tip prevent delamination or disbond due to peeling at the tip. Unfortunately, for most of the geometries currently in use, the use of pretensioned bolts cannot mitigate the crack initiation mechanism, but it can help the structure to provisionally arrest the crack propagation. This process is due to the end margin between the tip edge of the stringer termination and the axes of the last row of bolts, which is a mandatory design requirement. As shown in Fig. 6b, the area neighboring the tip is not affected by the through-thickness compressive stresses, which are localized in a small area surrounding the axes of the bolt. Hence the introduction of bolts is not beneficial to the structure in delaying the initial failure. Furthermore, bolts are not capable of relieving the sliding mode. Because of the end margin policy, significant transfer of the in-plane load happens in the area closely surrounding the run-out tip, where the bolts have no influence.

A possible improved version of this solution is shown schematically in Fig. 7. The use of the doublers could transfer the through-thickness compression to the tip datum plane, thus reducing the peeling stresses.

Unfortunately, assuming that the doublers are able to efficiently transfer the compressive stresses, they are not able to relieve the mode II components due to both the bending and the in-plane load resultants. Furthermore, the presence of back-to-back doublers is not suitable if the lower surface is external (e.g., skin/stringer assemblies in wings and horizontal/vertical tail planes).

As will be discussed in later sections, to maintain the *discrete* design, it is necessary to alter the mechanical and geometrical parameters to enforce the deformed shape to locally inhibit the excitement of at least one of the aforementioned failure modes.

As described in Fig. 8, the geometry can be tailored to locate the run-out tip near the zero-curvature point (Fig. 8b), thus inhibiting the failure subclasses due to the bending moment resultant.

Although tailoring all parameters could yield considerable increases in crack initiation loads, it is very difficult to predict the deformed shape with a reliable degree of confidence. In fact, the high nonlinearity of the problem, exacerbated especially in compressively loaded configurations, causes the actual shape to depend on the load level itself. The tailoring of geometrical and mechanical parameter needs to thoroughly assess the sensitivity of the deformed shape to the changes in boundary conditions and in external loads. If the stringer termination is designed to minimize the bending moment at the tip edge, the deformed shape needs to guarantee a certain degree of "stability," that is, the tip edge needs to be stable close to the

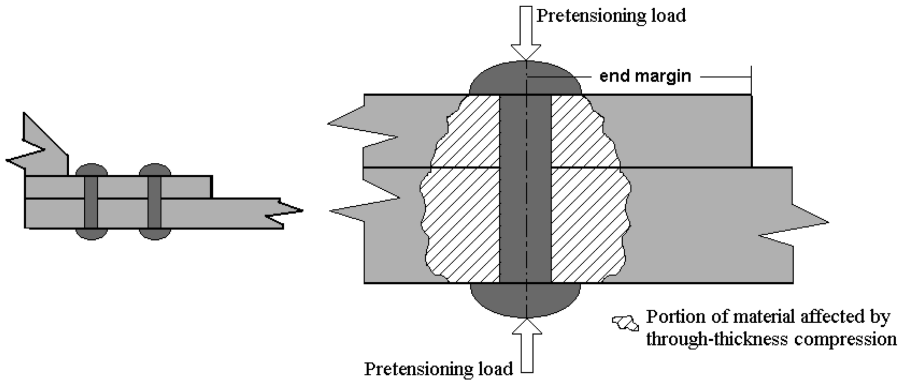

Fig. 6 a) Bolted end design solution and b) effect of pretensioning stresses.

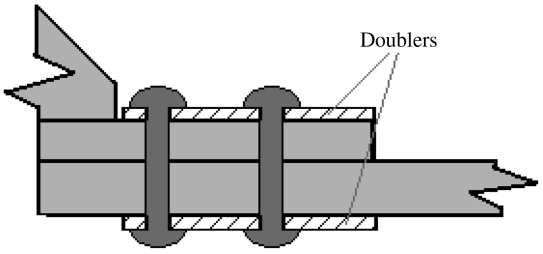

Fig. 7 Bolted end design solution with doublers.

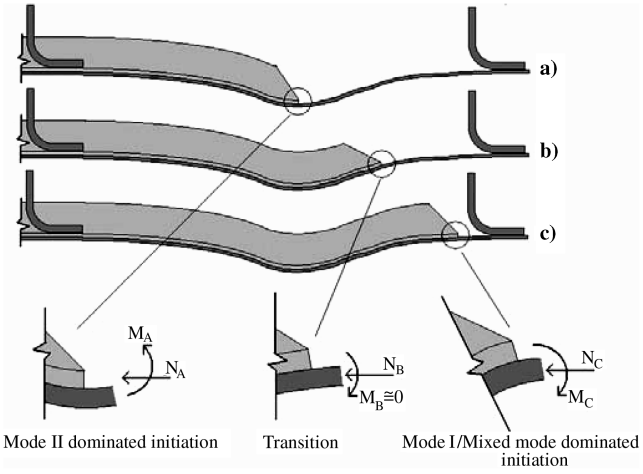

Fig. 8 Example of the effect of the termination tip span coordinate on the induced curvature, that is, on the transverse bending moment at the tip datum for stringer run-outs.

transition location (Fig. 8b), where the curvature is approximately zero. Furthermore, in compressive load cases, the stress concentration around the termination's tip can lead to local skin instabilities which could induce buckling of the portion of the skin facing the tip.

All of the described phenomena can be qualitatively captured by means of a detailed nonlinear analysis, for example, using the advanced ABAQUS nonlinear analysis combined with cohesive elements or the virtual crack closure technique to predict the disbond [7]. Unfortunately the current degree of reliability and robustness of such novel techniques in combination with the significant computational effort renders them not suitable for preliminary design and sizing purposes, when hundreds of different load cases need to be analyzed. Therefore, such techniques are suitable for virtual testing but not for being used as a sizing tool.

In light of the assumptions made (1–3), efforts to improve the mechanical response and increase the strain allowable are based on an attempt to partially relieve one of the three failure subclasses by adding structural components and optimizing the geometry. Further studies should be carried out to investigate alternative concepts of stringer termination, which requires more advanced means of analysis and might be more challenging from a manufacturing point of view, but this is beyond the scope of this article, which aims at finding an optimum solution for the discrete design concept. Nevertheless, it is the authors' intention to develop more comprehensive methods of analysis to assess a variety of novel design solutions.

II. Outline of the Approach

The present study aims at establishing a methodology to predict static initial failure loads of discrete composite stringer terminations and derive a series of guidelines for good design of such structures. The approach consists of two analytical models. The first model is a nonlinear approach, which provides the stress and displacement field throughout the domain of interest. This model represents the structure as a beam. The span length is the length of one single bay between two adjacent ribs; the maximum width is the foot width B_f. Effectively, the central strip is analyzed (see Fig. 9) and the in-plane load acting on the strip is derived as a fraction of the total external load acting on the panel, according to the total/strip axial stiffness ratio.

Both the left and the right ribs are assumed to restrain the structure inhibiting all degrees of freedom. The entire strip is considered to be isolated from the rest of the structure, meaning that apart from the ribs, no further mechanical restraints will be assumed in the present analysis. Geometrical properties and parameters, loads, and boundary conditions are shown in Fig. 10.

The nonlinear beam model is directly derived from the approach taken by the authors' previous work [1]. Expressions collapse to the one-dimensional case but a new set of base functions is employed to model the eccentricity to accurately capture the natural boundary conditions. The new formulation and complete set of equations are presented in Sec. III. The second model is based on a LEFM approach first proposed by Williams [6] for one-dimensional beam

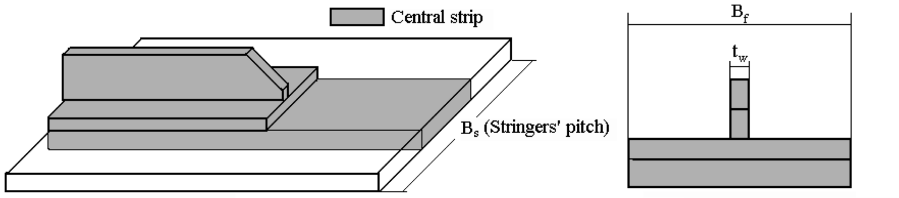

a) Region of interest **b) Central strip - cross section**

Fig. 9 Central strip definition: a) general representation; b) cross section.

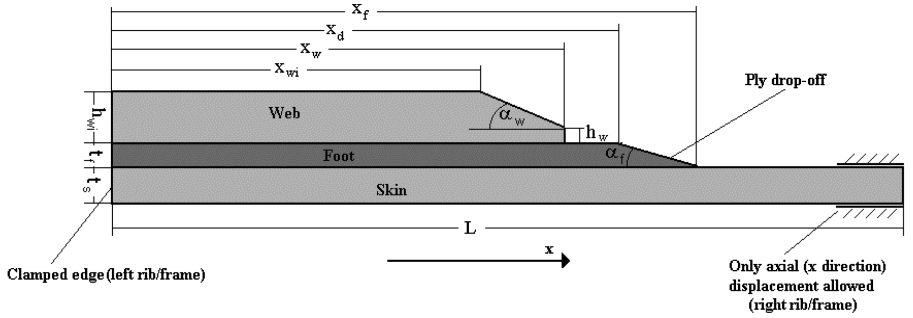

Fig. 10 Spanwise geometrical parameters.

analyses, enhanced in the present paper to account for ply drop-off. Closed form equations are presented to calculate the total strain energy release rate at the critical interfaces. The total contribution is then partitioned into its elementary contributions (excitations of modes I and II). A mode partitioning strategy is proposed to adjust Williams's formulation to capture the load sharing between skin and stringer at the run-out tip. Furthermore, a failure criterion is proposed [8] to predict crack initiation loads and to evaluate the actual reserve factor.

The LEFM model requires the bending moment and in-plane load at the run-out tip as input variables. These are calculated by means of the nonlinear beam model. Solving the nonlinear model results in the calculation of internal loads throughout the span, noting, however, that only the loads at the run-out tip are used in the LEFM model.

III. Governing Equations

The use of the modified von Kármán nonlinear approach [1], with the assumption of a constant in-plane load throughout the domain, guarantees that the governing equations can be expressed by means of one variable only, that is, the transverse deflection w. The membrane strain and the curvature are expressed as functions of the transverse displacement as follows:

$$\varepsilon = \frac{\partial u}{\partial x} + \frac{1}{2}\left(\frac{\partial w}{\partial x}\right)^2 \tag{1}$$

$$k = -\frac{\partial^2 w}{\partial x^2} \tag{2}$$

The constitutive equation relating bending moment and curvature of the laminated beam is

$$k = -\frac{M}{(EI)} \tag{3}$$

The beam is subjected to in-plane load N. Furthermore, the effect of a transverse load per unit length $q(x)$ is included in the model. Following, for example, Mansfield [9] and Kollar and Springer [10], the total strain energy U due to bending is

$$U = \frac{1}{2}\int_0^L (EI)k^2\,\mathrm{d}x = \frac{1}{2}\int_0^L (EI)\left(\frac{\mathrm{d}^2 w}{\mathrm{d}x^2}\right)^2 \mathrm{d}x \tag{4}$$

If the in-plane loads do not vary with x, the in-plane compatibility equation is identically satisfied and the potential Ω_N of external in-plane forces is [1,11]

$$\Omega_N = \frac{1}{2}\int_0^L N\left(\frac{\mathrm{d}w}{\mathrm{d}x} + \frac{\mathrm{d}e}{\mathrm{d}x}\right)^2 \mathrm{d}x \tag{5}$$

where $e(x)$ is the neutral plane function (describing eccentricity) which is treated as a moderately large initial perturbation, and N is the internal axial force equal to the external applied force. Similarly, the potential Ω_Q of the transverse load is [11]

$$\Omega_Q = -\int_0^{l_x} qw\,\mathrm{d}x \tag{6}$$

The total potential energy Π of the system is therefore

$$\Pi = U + \Omega_N + \Omega_Q \tag{7}$$

To properly exploit the Rayleigh–Ritz method, approximate expressions for the unknown variable w and for the eccentricity e are required. Expressions must satisfy the geometric boundary conditions. The following truncated series expansion satisfies the above conditions for transverse displacement and eccentricity:

$$w = \sum_{i=1}^{\bar{N}} \varphi_{w,i} w_i \tag{8}$$

$$e = \sum_{j=1}^{\bar{N}} \varphi_{e,j} e_j \tag{9}$$

The adopted shape functions $\varphi_{w,i}$ are the solutions of Euler's column buckling for a clamped/clamped beam [1]:

$$\varphi_{w,i}(x) = a_{1,i} + b_{1,i}x + c_{1,i}\sin\alpha_{1,i}x + d_{1,i}\cos\alpha_{1,i}x \tag{10}$$

where

$$a_{1,i} = -1 \tag{11a}$$

$$b_{1,i} = -\frac{\alpha_{1,i}L(\cos\alpha_{1,i}L - 1)}{\alpha_{1,i}L - \sin\alpha_{1,i}L} \tag{11b}$$

$$c_{1,i} = \frac{(\cos\alpha_{1,i}L - 1)}{\alpha_{1,i}L - \sin\alpha_{1,i}L} \tag{11c}$$

$$d_{1,m} = 1 \tag{11d}$$

The quantities $\alpha_{1,i}$ are the roots of the following transcendental equation:

$$\frac{\cos\lambda - 1}{\sin\lambda} - \lambda + \sin\lambda + \frac{\cos\lambda - 1}{\sin\lambda}\cos\lambda = 0 \tag{12a}$$

$$\lambda = \alpha L \tag{12b}$$

The shape functions $\varphi_{e,i}$ adopted to model the eccentricity are the eigenfunctions of a beam, which is clamped at $x = L$ and free at $x = 0$:

$$\varphi_{e,i}(x) = 1 - \cos\left[i\frac{\pi}{2L}(L - x)\right] \tag{13}$$

Coefficients e_i of the generalized series expansion are obtained by means of a Galerkin technique [1].

Substituting Eqs. (8) and (9) into Eqs. (4–6) the total potential is expressed as a second-order polynomial of the $\bar{N}$ unknown coefficients w_i. Expressions for U, Ω_N, and Ω_Q are described as follows:

$$U = \frac{1}{2}\left(\sum_{i=1}^{\bar{N}}\sum_{j=1}^{\bar{N}}\int_0^L (EI)\frac{\mathrm{d}^2\varphi_{w,i}}{\mathrm{d}x^2}\frac{\mathrm{d}^2\varphi_{w,j}}{\mathrm{d}x^2}\,\mathrm{d}x\right)w_i w_j \tag{14}$$

$$\begin{aligned}\Omega_N = &-\frac{1}{2}\left(\sum_{i=1}^{\bar{N}}\sum_{j=1}^{\bar{N}}\int_0^L N\varphi_{w,i}\varphi_{w,j}\,\mathrm{d}x\right)w_i w_j \\ &-\left(\sum_{i=1}^{N}\sum_{j=1}^{N}\int_0^L N\varphi_{w,i}\varphi_{e,i}\,\mathrm{d}x\right)w_i e_j \\ &-\frac{1}{2}\left(\sum_{i=1}^{\bar{N}}\sum_{j=1}^{\bar{N}}\int_0^L N\varphi_{e,i}\varphi_{e,j}\,\mathrm{d}x\right)e_i e_j\end{aligned} \tag{15}$$

$$\Omega_Q = -\left(\sum_{i=1}^{\bar{N}}\int_0^L q(x)\varphi_{w,i}\right)w_i \tag{16}$$

The principle of stationary potential energy states that

$$\frac{\partial \Pi}{\partial w_i} = 0, \quad \forall\ i = 1, \ldots, \bar{N} \tag{17}$$

Equations (14–16) are now substituted into Eq. (17) with the result differentiated with respect to w_i. Algebraic manipulations result in the following linear system of $\bar{N}$ equations in the $\bar{N}$ unknowns w_i, $i = 1, \ldots, \bar{N}$:

$$(\mathbf{G} + \mathbf{H})\mathbf{W} = -\bar{\mathbf{H}}\mathbf{E} + \mathbf{Q} \tag{18}$$

Vectors $\mathbf{Q}$, $\mathbf{E}$ and matrices $\mathbf{G}$, $\mathbf{H}$, and $\bar{\mathbf{H}}$ are defined as

$$\mathbf{Q}_i = \int_0^L q\phi_i \, \mathrm{d}x \, \mathrm{d}y \tag{19}$$

$$\mathbf{E} = [\, e_1 \quad e_2 \ldots \quad e_{M\times N}\,]^T \tag{20}$$

$$[\mathbf{G}]_{ij} = \int_0^L (EI) \frac{\mathrm{d}^2\varphi_{w,i}}{\mathrm{d}x^2} \frac{\mathrm{d}^2\varphi_{w,j}}{\mathrm{d}x^2} \, \mathrm{d}x \tag{21}$$

$$[\mathbf{H}]_{ij} = N \int_0^L \frac{\mathrm{d}\varphi_{w,i}}{\mathrm{d}x} \frac{\mathrm{d}\varphi_{w,j}}{\mathrm{d}x} \, \mathrm{d}x \tag{22}$$

$$[\bar{\mathbf{H}}]_{ij} = N \int_0^L \frac{\mathrm{d}\varphi_{w,i}}{\mathrm{d}x} \frac{\mathrm{d}\varphi_{e,j}}{\mathrm{d}x} \, \mathrm{d}x \tag{23}$$

The system described by Eq. (18) is invertible and yields the $\bar{N}$ coefficients w_i, which completely describe the state of stress and strain throughout the domain. The truncation causes an error, which is negligible if the number N of eigenfunctions used is reasonably large and guarantees the convergence of the approximate solution.

In general, for linear problems involving only transverse displacements due to external transverse loads, $\bar{N} = 5$ guarantees excellent convergence and degree of accuracy. For the present case, the presence of geometrical nonlinearities in conjunction with the discontinuity of the eccentricity extends the convergence threshold to a larger number of eigenfunctions, typically between 10 and 20 terms are required. An example of the calculation procedure is given and results are compared with a two-dimensional nonlinear finite element analysis (FEM). With reference to Figs. 9 and 10, geometry and material properties used are reported in Table 1. The series expansion was truncated at $\bar{N} = 20$. Out-of-plane displacements, rotations, and bending moments are compared and comparisons are shown in Fig. 11. The in-plane external load applied is $F = 10$ kN. Results show excellent correlation with FEM.

Table 1 Geometry and average elastic moduli

E_s, MPa	94,125
E_w, MPa	107,550
E_f, MPa	107,550
B_f, mm	70
L, mm	1,000
h_{wi}, mm	45
h_w, mm	6
t_s, mm	8
t_f, mm	4
t_w, mm	8
X_w, mm	300
X_f, mm	400
α_w, deg	30
α_f, deg	5

IV. Disbond Model

The disbond model is based on the theory first developed by Williams [6]. Several studies [1,12,13] have proven that the model is suitable for fast and reliable prediction of crack initiation. An analytical approach is fully developed to further improve the disbond model to allow for the calculation of the internal and external works when a stiffness gradient is present instead of an abrupt discontinuity (e.g., ply drop-offs, see Fig. 12).

The effect of tapering the foot tip is represented by replacing the tapered area with a foot termination of constant thickness and

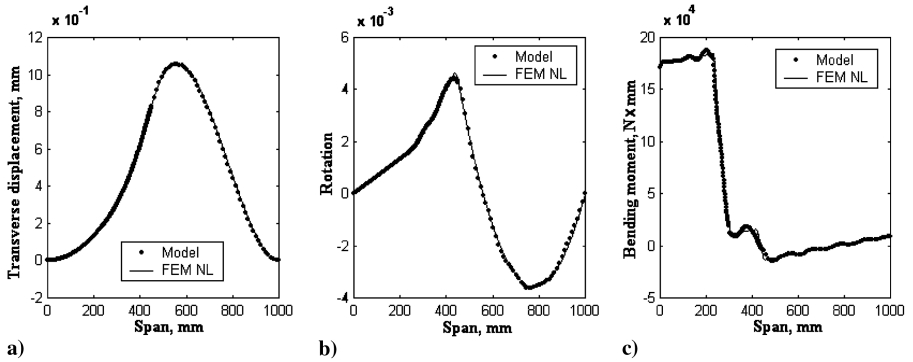

a) b) c)

Fig. 11 Spanwise correlation. a) Transverse displacement w; b) section rotation; c) bending moment; nonlinear (NL).

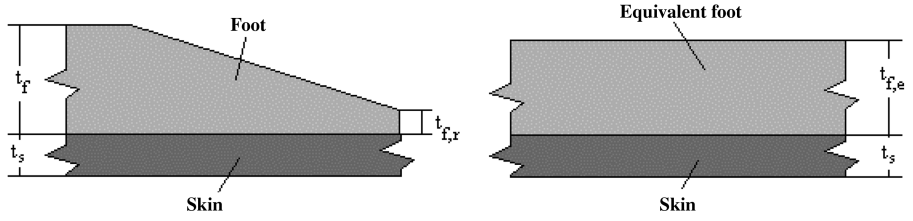

a) Real configuration **b) Equivalent scheme**

Fig. 12 Schematization of ply drop-offs.

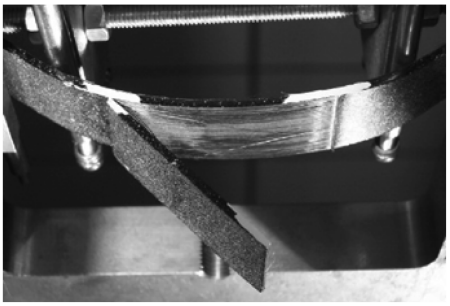

Fig. 13 Test fixture and final failure of four-points bending specimen.

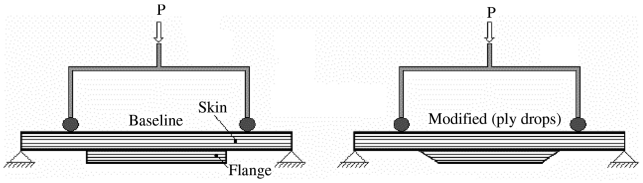

a) Baseline **b) Ply drop-off**

Fig. 14 Test configurations: a) baseline; b) ply drop-off.

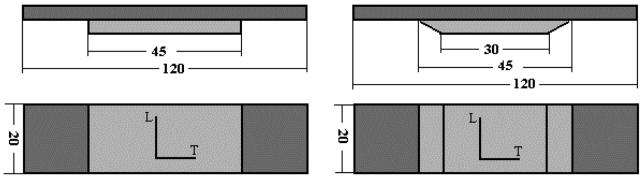

a) Baseline **b) Ply drop-off**

Fig. 15 Specimen dimensions: a) baseline; b) ply drop-off.

equivalent elastic modulus. Rationales for calculation of equivalent section properties are given in Appendix A. It is assumed that the critical location is the skin/foot bond line at the foot tip, where contributions to the local strain energy release rate due to the bending moment and in-plane load are expressed below for configurations with and without ply drop-offs. The presence of residual foot thickness $t_{f,r}$ is included in the model. Strain energy release rates given in Appendix A, are

$$G_I^M = \frac{(M_f - \Psi M_s)^2}{2B(1+\Psi)^2}\left[\frac{1}{(EI)_f} + \frac{1}{(EI)_s}\right] \tag{24a}$$

$$G_{II}^M = \frac{(M_f + M_s)^2}{2B(1+\Psi)^2}\left[\frac{1}{(EI)_f} + \frac{\Psi^2}{(EI)_s} - \frac{(1+\Psi)^2}{(EI)_{\text{tot}}}\right] \tag{24b}$$

Table 2 Test matrix

		No. of tests
Configuration 1	Baseline	4
	Ply drop-off	4
Configuration 2	Baseline	4
	Ply drop-off	4

$$G_I^F = 0 \tag{25a}$$

$$G_{II}^F = \frac{F^2}{2B}\left[\frac{1}{(EA)_s} - \frac{1}{(EA)_{\text{tot}}}\right] \tag{25b}$$

$$G_I^M = \frac{(M_f - \Psi_e M_s)^2}{2B(1+\Psi_e)^2}\left[\frac{1}{(EI)_{f,e}} + \frac{1}{(EI)_s}\right] \tag{26a}$$

$$G_{II}^M = \frac{(M_f + M_s)^2}{2B(1+\Psi_e)^2}\left[\frac{1}{(EI)_{f,e}} + \frac{\Psi_e^2}{(EI)_s} - \frac{(1+\Psi_e)^2}{(EI)_{\text{tot},e}}\right] \tag{26b}$$

$$G_I^F = 0 \tag{27a}$$

$$G_{II}^F = \frac{F^2}{2B}\left[\frac{1}{(EA)_s} - \frac{1}{(EA)_{\text{tot},e}}\right] \tag{27b}$$

A series of four point bending tests were conducted to validate the method and understand and quantify the benefit obtained by making use of the ply drop-off design. The test rig is depicted in Fig. 13. Test specimens are sketched in Fig. 14 and the test matrix is reported in Table 2. Skin and flange are co-bonded. Specimen's geometry is reported in Fig. 15. Material properties used for T700/M21 134 g/m^2 are as follows: $E_L = 119,680$ MPa; $E_T = 8500$ MPa; $G_{LT} = 4500$ MPa; and $\nu_{LT} = 0.32$. A total of 16 tests were performed. Two batches of four specimens were tested per each configuration.

Comparisons with tests are reported in Tables 3–5. It is noted that the model's predictions match test data closely. It is emphasized that a significant increase in failure loads can be obtained by taking advantage of ply drop-offs. The failure criterion used to predict failure is a quadratic power law [1] given by

$$\left(\frac{G_{\text{tot},I}}{G_{I,C}}\right)^2 + \left(\frac{G_{\text{tot},II}}{G_{II,C}}\right)^2 = 1 \tag{28}$$

Table 4 Comparison with tests results: Configuration 1

Configuration 1	Test[a] (mean values, four specimens)	Analytical[a]
Baseline	1	0.88
Ply drop-off	1.32	1.28

[a]Results divided by the mean value of the baseline batch.

Table 5 Comparison with tests results: Configuration 2

Configuration 2	Test[a] (mean values, four specimens)	Analytical[a]
Baseline	1	0.98
Ply drop-off	1.49	1.35

[a]Results divided by the mean value of the baseline batch.

Table 3 Specimen configurations

Nominal ply thickness: 0.13 mm	Configuration 1 stacking sequences	Configuration 2 stacking sequences
Skin	[90/45/0/ − 45/ − 45/0/45/0] s	[45/90/ − 45/0/ − 45/0/45/0] s
Flange	[90/45/0/0/ − 45/0/0] s	[45/0/ − 45/0/90/0/0] s

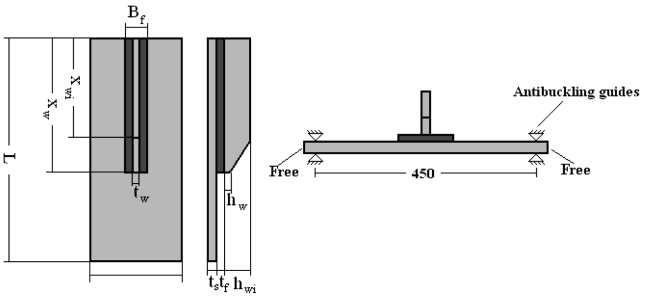

Fig. 16 Baseline specimen; dimensions are given in millimeters.

V. Model Validation

To validate the accuracy of the present model, five configurations were analyzed and results were compared with nonlinear FEM using ABAQUS [7]. Average elastic moduli were used for the skin, the stringer, and the foot. Boundary conditions are reported in Figs. 10 and 16. The specimen with the stringer terminated at midbay was taken as baseline. To evaluate the effect of terminating the stringer at different locations along the span, stringers in configurations A, B, C, and D (see Fig. 17) are terminated at 15, 35, 65, and 85% of the bay length, respectively. Virtual specimens were tested both in tension and in compression. Virtual specimens are briefly sketched in Figs. 16 and 17. Figure 18 shows details of the mesh used locally to model the bond line with cohesive elements (COH3D8). Geometrical and material properties are the same as reported in Table 1. Values used for critical strain energy release rates are as follows: $G_{1c} = 250\ \mathrm{J/m^2}$ and $G_{2c} = 1100\ \mathrm{J/m^2}$. Results are compared in Table 6. Rationales on the application of the LEFM model at the run-out tip are provided in Appendix B.

Results show fairly good correlation between the present model and ABAQUS predictions. The discrepancy found for configuration A can be attributed to the failure predicted by the FEM at the corner of the foot. The present method is based on a one-dimensional strip analysis and therefore it cannot capture failure modes due to local effects such as stress concentration at free corners.

VI. Conclusions

A robust and efficient method for a quick evaluation of stringer run-outs critical failure mode is presented. Comparison with detailed FEM shows that the method is reasonably accurate. Despite limitations due to one-dimensional assumptions, failure modes are well captured by the model. The proposed approach provides significantly more efficient analysis of the fracture of stiffened panels than those others commonly used. If used for industrial purposes, its accuracy must and can be improved by taking into account the effect of the second dimension (which causes biaxial loadings that cannot be accounted for by the present analysis) to fit with test results, and also defining knockdown factors to render the predictions conservative for all the comparisons. The approach typically works well for stiffened panels with symmetric stiffeners for which there is an abrupt run-out or a ply drop-off. The main limitations of the analysis are as follows:

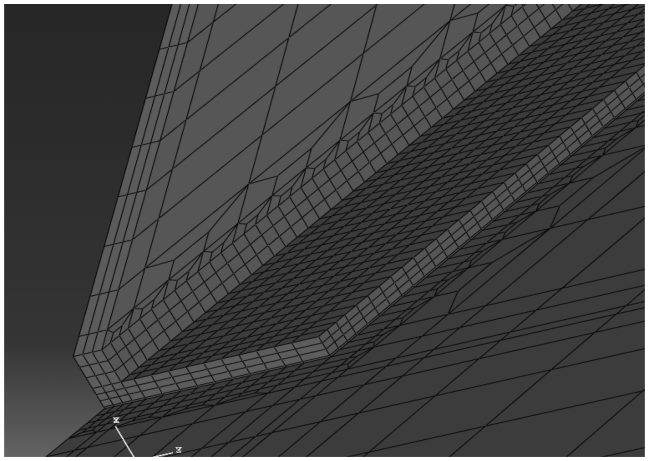

Fig. 18 ABAQUS model. Local mesh at the run-out tip.

1) The method schematizes the panel as a beam. Only axial load (parallel to stringer direction) and transverse pressure can be applied. Biaxial and in-plane loading contributions are not represented.

2) Only open-sectioned stringers are considered (e.g., T or L stringers). Closed sections, such as trapezoidal stringers, are not yet represented by the present method.

3) Only classical discrete configurations are modeled. Integral stringer concept or internal pad-ups cannot be modeled by means of the present analysis.

4) Stress concentrations due to the free edge of the stringer foot or corner effect as well as uneven stress distribution along the very tip edge are not accounted for. Empirical knockdown factors could be derived from tests and used to render the method conservative.

Appendix A: Ply Drop-Off Analytical Formulation

To account for ply drop-off, local strain energies [1,6] $U_{\mathrm{DO},M}$ and $U_{\mathrm{DO},N}$ of the drop-off area (Fig. A1d) are calculated under two different assumptions: constant strain and constant curvature (Figs. A1e and A1f, respectively). Results are then compared to local strain energies U_M and U_N of a configuration without ply drop-off (Fig. A1a), calculated over the same region and under identical assumptions, that is, same constant curvature and longitudinal strain (Figs. A1b and A1c, respectively). Hence correction factors C_M and C_N are derived for strain energy and external work done by moment and in-plane load.

The total strain energy stored in the drop-off region under the assumption of a constant curvature k is

$$U_{\mathrm{DO},M} = \frac{1}{2}\int_0^{l_{\mathrm{DO}}} k^2 E_f I(x)\,\mathrm{d}x = \frac{1}{8}\frac{k^2 E_f B}{12\tan(\alpha)}(t_f^4 - t_r^4) \qquad \text{(A1)}$$

The total strain energy stored in the drop-off region under the assumption of a constant axial strain ε is

$$U_{\mathrm{DO},N} = \frac{1}{2}\int_0^{l_{\mathrm{DO}}} \varepsilon^2 E_f A(x)\,\mathrm{d}x = \frac{1}{4}\frac{\varepsilon^2 E_f B}{\tan(\alpha)}(t_f^2 - t_r^2) \qquad \text{(A2)}$$

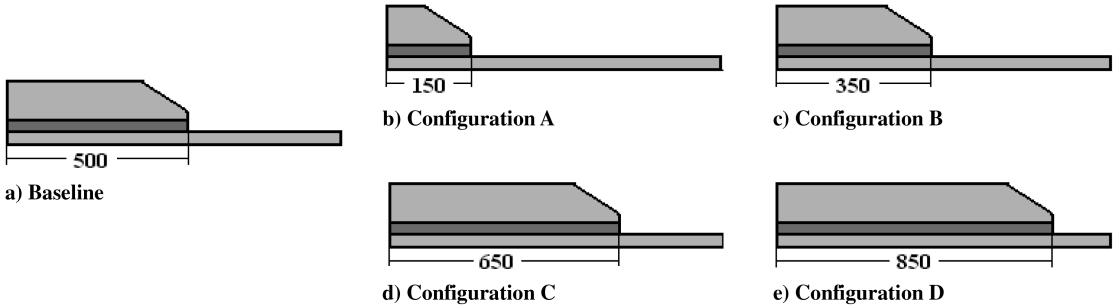

Fig. 17 Virtual specimens; dimensions are given in millimeters.

Table 6 Results comparison

Configuration	Failure loads (crack initiation), kN			
	Tension		Compression	
	ABAQUS	Present	ABAQUS	Present
A	652	600	691	594
B	591	594	629	595
Baseline	551	576	548	578
C	560	521	574	537
D	549	516	563	534

The total strain energies stored in the reference configuration under the assumptions of constant curvature k and constant axial strain ε are

$$U_M = \frac{1}{2}\int_0^{l_{DO}} k^2 E_f I \, dx = \frac{1}{2}\frac{k^2 E_f B}{12} t_f^3 l_{DO} \tag{A3}$$

$$U_N = \frac{1}{2}\int_0^{l_{DO}} \varepsilon^2 E_f A \, dx = \frac{1}{2}\varepsilon^2 E_f B t_f l_{DO} \tag{A4}$$

Defining the following correction factors:

$$C_M = \frac{U_{DO,M}}{U_M} = \frac{1}{4}\frac{t_f^4 - t_r^4}{t_f^3(t_f - t_r)} \tag{A5}$$

$$C_N = \frac{U_{DO,N}}{U_N} = \frac{1}{2}(t_f - t_r) \tag{A6}$$

one can express strain energy stored in the drop-off region as a fraction of the strain energy stored in the reference configuration:

$$U_{DO,M} = C_M U_M \tag{A7}$$

$$U_{DO,N} = C_N U_N \tag{A8}$$

Two parameters $t_{f,e}$ and $E_{f,e}$ are introduced to define an equivalent beam (Fig. A1g). The parameters are determined by imposing the condition that the total strain energies stored in the equivalent beam undergoing the same constant curvature ($U_{e,M}$) and axial strain ($U_{e,N}$) equal $U_{DO,M}$ and $U_{DO,N}$, respectively,

$$U_{e,M} = C_M U_M \tag{A9}$$

$$U_{e,N} = C_N U_N \tag{A10}$$

$U_{e,M}$ and $U_{e,N}$ are (Figs. A1h and A1i) calculated as follows:

$$U_{e,M} = \frac{1}{2}\int_0^{l_{DO}} k^2 E_{f,e} I_e \, dx = \frac{1}{2}\frac{k^2 E_{f,e} B}{12} t_{f,e}^3 l_{DO} \tag{A11}$$

$$U_N = \frac{1}{2}\int_0^{l_{DO}} \varepsilon^2 E_f A_e \, dx = \frac{1}{2}\varepsilon^2 E_{f,e} B t_{f,e} l_{DO} \tag{A12}$$

Substituting Eqs. (A5) and (A6) into Eqs. (A9) and (A10) and then into Eqs. (A11) and (A12), the following relations are derived for equivalent bending and axial stiffness:

$$(EI)_{f,e} = C_M (EI)_f \tag{A13}$$

$$(EA)_{f,e} = C_N (EA)_f \tag{A14}$$

Equivalent thickness and elastic modulus are then calculated as follows:

$$E_{f,e} = \frac{1}{2\sqrt{3}B}(C_M)^{-1/2}(C_N)^{3/2}\sqrt{\frac{(EA)_f}{(EI)_f}}(EA_f) \tag{A15}$$

$$t_{f,e} = 2\sqrt{3}(C_M)^{1/2}(C_N)^{1/2}\sqrt{\frac{(EI)_f}{(EA)_f}} \tag{A16}$$

Strain energy release rates due to bending moment and in-plane load [1,6] are expressed as (see Fig. 12)

$$G_I^M = \frac{(M_{f,e} - \Psi_e M_s)^2}{2B(1+\Psi_e)^2}\left[\frac{1}{(EI)_{f,e}} + \frac{1}{(EI)_s}\right] \tag{A17a}$$

$$G_{II}^M = \frac{(M_{f,e} + M_s)^2}{2B(1+\Psi_e)^2}\left[\frac{1}{(EI)_{f,e}} + \frac{\Psi_e^2}{(EI)_s} - \frac{(1+\Psi_e)^2}{(EI)_{\text{tot},e}}\right] \tag{A17b}$$

$$G_I^F = 0 \tag{A18a}$$

$$G_{II}^F = \frac{F^2}{2B}\left[\frac{1}{(EA)_s} - \frac{1}{(EA)_{\text{tot},e}}\right] \tag{A18b}$$

where

$$\Psi_e = \frac{(EI)_s}{(EI)_{f,e}} \tag{A19}$$

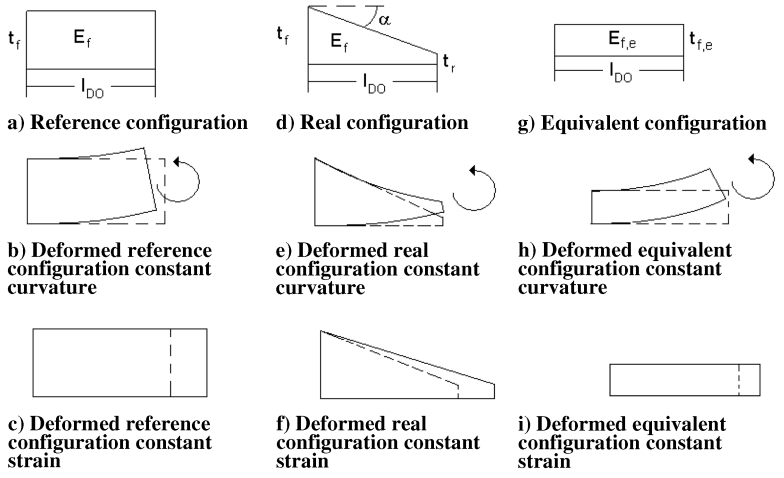

a) Reference configuration **d) Real configuration** **g) Equivalent configuration**

b) Deformed reference configuration constant curvature **e) Deformed real configuration constant curvature** **h) Deformed equivalent configuration constant curvature**

c) Deformed reference configuration constant strain **f) Deformed real configuration constant strain** **i) Deformed equivalent configuration constant strain**

Fig. A1 Drop-off area idealization.

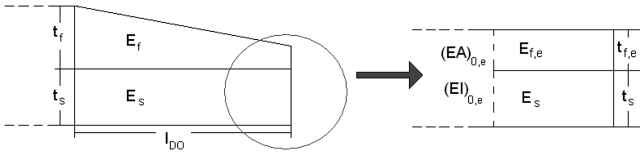

a) Real configuration b) Local schematization

Fig. A2 Local idealization.

Quantities $(EA)_{0,e}$ and $(EI)_{0,e}$ are calculated according to the geometry shown in Fig. A2, once $E_{f,e}$ and $t_{f,e}$ are known.

Appendix B: Modal Contributes Partitioning

To proper employ the disbond model, an appropriate partition of load is required. Referring to the free-body schemes in Fig. B1, the loads exchanged between the overlap section (skin/foot) and the skin can be partitioned into three distinct components.

1) M_r, due to local curvature of the skin, is exchanged between the two sections and acts only on the lower adherend of the joint (skin part).

2) N, due to the external in-plane load acting on the lower adherend of the joint (skin part). It is introduced from the skin into the skin–stringer region.

3) The discontinuous increment ΔM, due to the local eccentricity. It acts on the whole overlap section only.

The in-plane load N triggers mode II excitation only. Referring to Williams [6], mode partitioning is obtained as

$$G_I^N = 0 \tag{B1a}$$

$$G_{II}^N = \frac{N^2}{2B}\left[\frac{1}{(EA)_s} - \frac{1}{(EA)_{\text{tot}}}\right] \tag{B1b}$$

where

$$(EA)_{\text{tot}} = (EA)_s + (EA)_f \tag{B2}$$

or, in the case of ply drop-off:

$$G_I^N = 0 \tag{B3a}$$

$$G_{II}^N = \frac{N^2}{2B}\left[\frac{1}{(EA)_s} - \frac{1}{(EA)_{\text{tot},e}}\right] \tag{B3b}$$

where

$$(EA)_{\text{tot}}, e = (EA)_s + (EA)_{f,e} \tag{B4}$$

The bending moment due to local eccentricity ΔM triggers mode II excitation only. Referring to Williams [6] and Dahlen and Springer [13], mode partitioning is obtained as

$$G_I^{\Delta M} = \frac{(\Delta M_s - \Psi \Delta M_f)^2}{2B(1+\Psi)^2}\left[\frac{1}{(EI)_f} + \frac{1}{(EI)_s}\right] \tag{B5a}$$

$$G_{II}^{\Delta M} = \frac{(\Delta M_s + \Delta M_f)^2}{2B(1+\Psi)^2}\left[\frac{1}{(EI)_f} + \frac{\Psi^2}{(EI)_s} - \frac{(1+\Psi)^2}{(EI)_{\text{tot}}}\right] \tag{B5b}$$

or, in the case of ply drop-off:

$$G_I^{\Delta M} = \frac{(\Delta M_s - \Psi_e \Delta M_f)^2}{2B(1+\Psi_e)^2}\left[\frac{1}{(EI)_{f,e}} + \frac{1}{(EI)_s}\right] \tag{B6a}$$

$$G_{II}^{\Delta M} = \frac{(\Delta M_s + \Delta M_f)^2}{2B(1+\Psi_e)^2}\left[\frac{1}{(EI)_{f,e}} + \frac{\Psi_e^2}{(EI)_s} - \frac{(1+\Psi_e)^2}{(EI)_{\text{tot},e}}\right] \tag{B6b}$$

It is assumed that after the initial virtual crack da (Fig. B2), the bending moments are partitioned between the skin and the foot proportionally to their bending stiffnesses. Upper (foot) and lower (skin) components can be derived assuming that both parts have the same curvature after crack initiation, and applying the bending moment equilibrium of the free body

$$\Delta M_f + \Delta M_s = \Delta M_{\text{tot}} \tag{B7a}$$

$$\frac{\Delta M_f}{(EI)_f} = \frac{\Delta M_s}{(EI)_s} \tag{B7b}$$

or, in the case of ply drop-off

$$\Delta M_f + \Delta M_s = \Delta M_{\text{tot}} \tag{B8a}$$

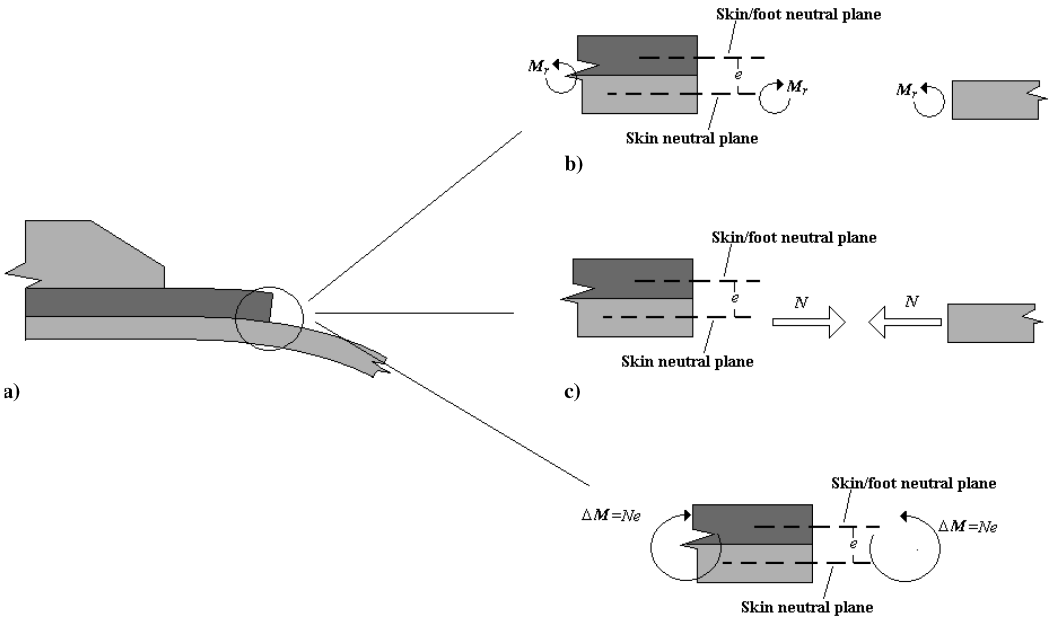

Fig. B1 Local free bodies.

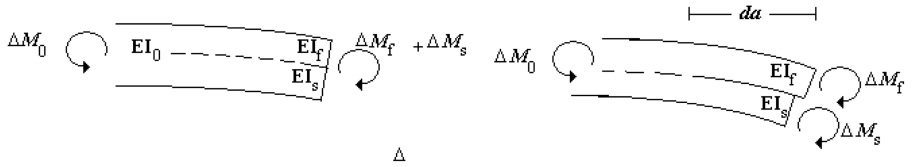

a) Induced increment (before initial crack) **b) Induced increment (after initial crack)**

Fig. B2 Incremental bending moment partitioning.

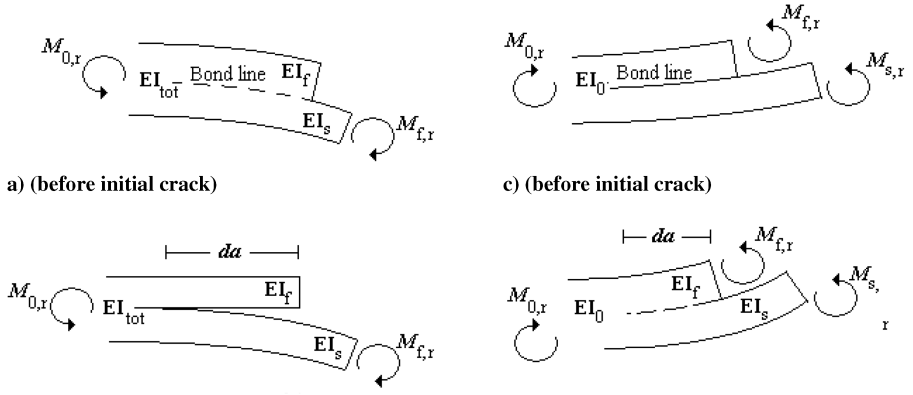

a) (before initial crack) **c) (before initial crack)**

b) (after initial crack) **d) (after initial crack)**

Fig. B3 Partitioning of bending moment due to local skin curvature.

$$\frac{\Delta M_f}{(EI)_{f,e}} = \frac{\Delta M_s}{(EI)_s} \tag{B8b}$$

Substituting Eqs. (B7b) and (B8b) into Eqs. (B5a) and (B6a) yields a zero mode I excitation.

Local bending M_r due to skin curvature can either trigger mode II excitation only or a mixed mode contribution. Referring to Fig. B3, if the local curvature of the skin at the run-out tip is negative (Figs. B3a and B3b), only mode I and mode II contributions are present. If the local curvature of the skin at the run-out tip is positive (Figs. B3c and B3d), only a mode II contribution is present.

In the case of negative curvature, contributions are

$$G_I^{M_r} = \frac{(M_{r,s} - \Psi M_{r,f})^2}{2B(1+\Psi)^2}\left[\frac{1}{(EI)_f} + \frac{1}{(EI)_s}\right] \tag{B9a}$$

$$G_{II}^{M_r} = \frac{(M_{r,f} + M_{r,s})^2}{2B(1+\Psi)^2}\left[\frac{1}{(EI)_f} + \frac{\Psi^2}{(EI)_s} - \frac{(1+\Psi)^2}{(EI)_{\text{tot}}}\right] \tag{B9b}$$

or, in the case of ply drop-off

$$G_I^{M_r} = \frac{(M_{r,s} - \Psi_e M_{r,f})^2}{2B(1+\Psi_e)^2}\left[\frac{1}{(EI)_{f,e}} + \frac{1}{(EI)_s}\right] \tag{B10a}$$

$$G_{II}^{M_r} = \frac{(M_{r,f} + M_{r,s})^2}{2B(1+\Psi_e)^2}\left[\frac{1}{(EI)_{f,e}} + \frac{\Psi_e^2}{(EI)_s} - \frac{(1+\Psi_e)^2}{(EI)_{\text{tot},e}}\right] \tag{B10b}$$

where

$$M_{r,s} = M_{r,0} \tag{B11a}$$

$$M_{r,f} = 0 \tag{B11b}$$

In the case of positive curvature, assumptions made for ΔM still hold; hence expressions for mode partitioning are

$$G_I^{M_r} = \frac{(M_{r,s} - \Psi M_{r,f})^2}{2B(1+\Psi)^2}\left[\frac{1}{(EI)_f} + \frac{1}{(EI)_s}\right] \tag{B12a}$$

$$G_{II}^{M_r} = \frac{(M_{r,f} + M_{r,s})^2}{2B(1+\Psi)^2}\left[\frac{1}{(EI)_f} + \frac{\Psi^2}{(EI)_s} - \frac{(1+\Psi)^2}{(EI)_{\text{tot}}}\right] \tag{B12b}$$

or, in the case of ply drop-off

$$G_I^{M_r} = \frac{(M_{r,s} - \Psi_e M_{r,f})^2}{2B(1+\Psi_e)^2}\left[\frac{1}{(EI)_{f,e}} + \frac{1}{(EI)_s}\right] \tag{B13a}$$

$$G_{II}^{M_r} = \frac{(M_{r,f} + M_{r,s})^2}{2B(1+\Psi_e)^2}\left[\frac{1}{(EI)_{f,e}} + \frac{\Psi_e^2}{(EI)_s} - \frac{(1+\Psi_e)^2}{(EI)_{\text{tot},e}}\right] \tag{B13b}$$

where

$$M_{r,f} + M_{r,s} = M_{r,o} \tag{B14a}$$

$$\frac{M_{r,f}}{(EI)_f} = \frac{\Delta M_{r,s}}{(EI)_s} \tag{B14b}$$

or, in the case of ply drop-off

$$M_{r,f} + M_{r,s} = M_{r,o} \tag{B15a}$$

$$\frac{M_{r,f}}{(EI)_{f,e}} = \frac{\Delta M_{r,s}}{(EI)_s} \tag{B15b}$$

Again, substituting Eqs. (B14b) and (B15b) into Eqs. (B12a) and (B13a) yields a zero mode I excitation.

Acknowledgments

The first author would like to thank Matthew Beard (Airbus UK, Ltd.) for the financial support provided. Furthermore, the first author would like to express gratitude to Jean-Luc Leon Dufour,

Henrik Roesner, and Edward Hunt (Airbus UK, Ltd.) for their precious support and valuable comments.

References

[1] Cosentino, E., and Weaver, P. M., "Approximate Non-Linear Analysis Method for Debonding of Skin/Stringer Composite Assemblies," *AIAA Journal*, Vol. 46, No. 5, May 2008, pp. 1144–1159. doi:10.2514/1.31914

[2] Volpert, Y., and Gottesman, T., "Skin-Stiffener Interface Stresses in Tapered Composite Panel," *Composite Structures*, Vol. 33, 1995, pp 1–6. doi:10.1016/0263-8223(95)80025-5

[3] Falzon, B. J., and Davies, G. A. O., "The Behavior of Compressively Loaded Stiffener Runout Specimens—Part 2: Finite Element Analysis," *Journal of Composite Materials*, Vol. 37, No. 6, 2003, pp. 481–501. doi:10.1177/0021998303037006416

[4] Meeks, C., Greenhalgh, E., and Falzon, B., "Stiffener Debonding Mechanism in Post Buckled CFRP Aerospace Plates," *Composites, Part A: Applied Science and Manufacturing*, Vol. 36, 2005, pp 934–946. doi:10.1016/j.compositesa.2004.12.003

[5] Greenhalgh, E., and Huertas-Garcia, M., "Fracture Mechanics and Failure Processes at Stiffener Run-Outs in Polymer Matrix Composite Stiffened Elements," *Composites, Part A: Applied Science and Manufacturing*, Vol. 35, 2004, pp. 1447–1458. doi:10.1016/j.compositesa.2004.05.006

[6] Williams, J. G., "On the Calculation of Energy Release Rates for Cracked Laminates," *International Journal of Fracture*, Vol. 36, 1988, pp. 101–119. doi:10.1007/BF00017790

[7] ABAQUS Ver. 6.5.1, User Manual, Vol. 4, ABAQUS Inc., 2004.

[8] Wu, F. W., "Application of Fracture Mechanics to Anisotropic Plates," *Journal of Applied Mechanics*, Vol. 34, Dec. 1968, pp. 967–974.

[9] Mansfield, E. H., *The Bending and Stretching of Plates*, 2nd ed., Cambridge Univ. Press, Cambridge, England, U.K., 1989, pp. 85–90.

[10] Kollar, L. P., and Springer, G. S., *Mechanics of Composite Structures*, Cambridge Univ. Press, Cambridge, England, U.K., 2003, Chap. 4.

[11] Timoshenko, S. P., and Gere, J., *Theory of Elastic Stability*, 2nd ed., McGraw–Hill, New York, 1961, pp. 55, 349.

[12] Taki, T., and Kitagawa, T., "Post-Buckling Strength of Composite Stiffened Panel Under Shear Load," AIAA Paper 95-393, 1995.

[13] Dahlen, C., and Springer, G. S., "Delamination Growth in Composites Under Cyclic Loads," *Journal of Composite Materials*, Vol. 28, No. 8, 1994, pp. 732–781.

R. Kapania
Associate Editor